Commun. Comput. Phys.
doi: 10.4208/cicp.OA-2018-0199

Vol. **28**, No. 1, pp. 328-341
July 2020

Source-Independent Amplitude-Semblance Full-Waveform Inversion using a Hybrid Time- and Frequency-Domain Approach

Benxin Chi* and Lianjie Huang

Geophysics Group, Los Alamos National Laboratory, Los Alamos, NM 87545, USA.

Received 8 August 2018; Accepted (in revised version) 14 January 2019

Abstract. Full-waveform inversion is a promising tool to produce accurate and high-resolution subsurface models. Conventional full-waveform inversion requires an accurate estimation of the source wavelet, and its computational cost is high. We develop a novel source-independent full-waveform inversion method using a hybrid time- and frequency-domain scheme to avoid the requirement of source wavelet estimation and to reduce the computational cost. We employ an amplitude-semblance objective function to not only effectively remove the source wavelet effect on full-waveform inversion, but also to eliminate the impact of the inconsistency of source wavelets among different shot gathers on full-waveform inversion. To reduce the high computational cost of full-waveform inversion in the time domain, we implement our new algorithm using a hybrid time- and frequency-domain approach. The forward and backward wave propagation operations are conducted in the time domain, while the frequency-domain wavefields are obtained during modeling using the discrete-time Fourier transform. The inversion process is conducted in the frequency domain for selected frequencies. We verify our method using synthetic seismic data for the Marmousi model. The results demonstrate that our novel source-independent full-waveform inversion produces accurate velocity models even if the source signature is incorrect. In addition, our method can significantly reduce the computational time using the hybrid time- and frequency-domain approach compared to the conventional full-waveform inversion in the time domain.

AMS subject classifications: 86A15, 86A22

Key words: Amplitude semblance, full-waveform inversion, hybrid time and frequency domain, source independent, source wavelet.

1 Introduction

Full-waveform inversion (FWI) is a highly nonlinear inversion process that inverts seismic data for an optimal subsurface model by minimizing the data misfit between ob-

*Corresponding author. *Email addresses:* benxin.chi@gmail.com (B. Chi), ljh@lanl.gov (L. Huang)

served and synthetic data [12, 22, 23]. Studies show that a well estimated source wavelet is one of the most important prerequisites for successful full-waveform inversion. This condition, however, is usually difficult to be satisfied in field data applications because of problems such as noises, imperfect receiver coupling, or unpreserved amplitudes during data processing, etc. Furthermore, when a subsurface model is inaccurate during inversion, it could be difficult to distinguish the contribution of the inaccurate model to the inversion objective function from that of the inaccurate source wavelet. An incorrect source wavelet, even with small-amplitude deviations from the true source wavelet, may yield obvious artifacts in inversion results, and FWI with an incorrect source wavelet can easily converge to a local minimum [17].

The estimation of source wavelet is therefore generally considered as an essential step in FWI but very challenging because of attenuation and noise, among others. In field data applications, the source wavelet can be obtained by extracting the source signature from direct-arrival waves, assuming either zero or minimum phase. However, the fidelity of the estimated wavelet depends greatly on assumptions used. In shallow marine explorations, the extraction of the source wavelet is very challenging when direct-arrival waves interfere with seismic reflections from the shallow water bottom. Another approach is to estimate the source signature by simultaneously inverting for model parameters and the source wavelet [22]. By taking the derivative of the misfit function with respect to the source wavelet, Zhou et al. [28] presented a source inversion in the time domain, while Pratt [11] developed a source inversion algorithm in the frequency domain. Although there have been some successful applications of this strategy [6, 7, 13, 14], an FWI that simultaneously inverts for these two quantities could easily fail to achieve reliable convergence when low-frequency components of data are not available, or the starting model is significantly different from the true model [25]. This is because the source wavelet and the subsurface velocity model are updated simultaneously, and the inaccuracy in both quantities can affect each other during inversion [3].

To alleviate the source wavelet effect on FWI, some source-independent FWI algorithms were developed [2,4,5,8,25–27]. In these methods, they used data convolved with or deconvolved by an optimized reference trace to construct a misfit function, and the influence of an inaccurate source wavelet on FWI can be partially suppressed. A fundamental issue resting in these methods is how to choose a good reference trace. In practice, the preferred reference position would be as close to the shot position as possible, because the anisotropic effects and non-linearity of wavefields increase and the signal-to-noise ratio is also lower in the far-offset data [2, 3]. For deconvolution-type misfit functions, a bad reference trace can devastate the deconvolution process and lead to singular values in the normalization process.

We develop a novel source-independent full-waveform inversion method without using an optimized reference trace. We employ an amplitude-semblance objective function to completely remove the necessity of source wavelet estimation in FWI. The most striking feature of our amplitude-semblance FWI (ASFWI) is that there is no need to manually choose a reference trace. The other obvious advantage of our ASFWI is that

it can effectively handle the inconsistency of different sources, including the excitation time, the center frequency, the excitation energy, and the excitation type, all of which may vary from source to source in field seismic data. In addition, we implement our new source-independent FWI algorithm in the hybrid time and frequency domain [15], that is, we perform forward and backward wave propagation operations in the time domain for easy parallel computing, compute the frequency-domain wavefields using the discrete-time Fourier transform during wavefield propagation, and carry out FWI in the frequency domain. One advantage of our new FWI method is that it removes the necessity of forward wavefield reconstruction, using either the boundary wavefield saving method [20] or the optimal checking point method [18]. Therefore, our new FWI is efficient in both the computational time and computer memory cost. Another advantage of our hybrid time- and frequency-domain FWI is that it is straightforward to successively invert from low to high frequencies, which mitigates the cycle skipping problems. We verify the effectiveness of our ASFWI using synthetic seismic data for the Marmousi model. The results demonstrate that our new method does not require an accurate source wavelet to produce efficiently an accurate and high-resolution inversion result.

In the Methodology section of our paper, we first describe the hybrid time- and frequency-domain FWI framework, define the source-independent amplitude-semblance FWI objective function, and derive the gradient based on this new objective function. We use a simple Gaussian anomaly example to verify the source-independent characteristics of our new FWI objective function. In the Numerical Examples section, we use synthetic seismic data from the Marmousi model to demonstrate the source-wavelet independence of our FWI method and its computational efficiency. We conclude our paper in the Conclusions section.

2 Methodology

2.1 FWI in the hybrid time and frequency domain

FWI using the hybrid time- and frequency-domain approach performs forward and backward wavefield propagation operations in the time domain, computes the frequency-domain wavefields during the wavefield modeling, and performs inversion in the frequency domain [15, 24].

We perform numerical modeling of acoustic-wave propagation in the time domain using an optimized high-order staggered-grid finite-difference algorithm with convolutional perfectly matched absorbing-boundary layers [19, 21]

$$\left[\frac{1}{K(\mathbf{x})}\frac{\partial^2}{\partial t^2}-\nabla\cdot\left(\frac{1}{\rho(\mathbf{x})}\nabla\right)\right]u(\mathbf{x},t)=f(\mathbf{x}_s,t), \tag{2.1}$$

where $\rho(\mathbf{x})$ is the density at spatial location $\mathbf{x}$, $K(\mathbf{x})$ is the bulk modulus, $f(\mathbf{x}_s,t)$ is the source term, $\mathbf{x}_s$ is the source location, $u(\mathbf{x},t)$ is the pressure wavefield and t represents time.

To compute the frequency wavefield at each subsurface grid point, we employ the discrete-time Fourier transform at each time step of time-domain wavefield modeling using

$$u(\omega)=\sum_{t=0}^{T}u(t)e^{i\omega t}, \tag{2.2}$$

where $u(\omega)$ is the mono-frequency wavefield at the frequency ω and T is the total recording time.

FWI in the hybrid time and frequency domain performs inversion in the frequency domain using only a few numbers of selected frequencies for inversion [16]. It is not necessary for this hybrid-domain FWI to solve the frequency-domain wave equations, which is not easily implemented on parallel computers and is computationally prohibitive for large-scale 3D models [9,10]. The time-domain modeling used in the hybrid-domain FWI can be easily parallelized on either CPUs or GPUs, like the time-domain FWI. The time-domain FWI requires three modeling operations. By contrast, the hybrid-domain FWI needs only two modeling operations because it does not need the wavefield reconstruction using either the boundary-wavefield-saving approach or the optimal check point approach and consequently, reduces the computational cost and the computer memory requirement (for saving the boundary wavefields).

The objective function for the hybrid-domain FWI at a given frequency ω is defined as

$$E(\mathbf{m})=\sum_{i=1}^{N_s}\sum_{j=1}^{N_r}\frac{1}{2}(u_{ij}-d_{ij})^*(u_{ij}-d_{ij}), \tag{2.3}$$

where u_{ij} and d_{ij} are synthetic and observed data for the i^{th} shot and j^{th} receiver, N_s is the total number of shots, and N_r is total number of receivers,and the superscript "$*$" denotes the complex conjugate. In the frequency domain, seismic data can be expressed as the multiplication of Green's function with a source wavelet. Therefore, the objective function in Eq. (2.3) is equivalent to

$$E(\mathbf{m})=\sum_{i=1}^{N_s}\sum_{j=1}^{N_r}\frac{1}{2}(g_{ij}^{u}s_i^{u}-g_{ij}^{d}s_i^{d})^*(g_{ij}^{u}s_i^{u}-g_{ij}^{d}s_i^{d}), \tag{2.4}$$

where g_{ij}^{u} and g_{ij}^{d} are Green's functions for synthetic and observed data, and s_i^{u} and s_i^{d} are source wavelets of synthetic and observed data for the i^{th} shot.

FWI minimizes the misfit function in Eq. (2.4) to update subsurface model parameters using source wavelets for all sources. The source wavelets should be estimated from seismic data before FWI. An incorrect source wavelet used in FWI, even with small amplitude and phase deviations from the true source wavelet, can lead to significant inversion artifacts and convergence to a local minimum.

The gradient vector of the objective function with respect to the model parameters is

obtained using adjoint state method [12, 22, 23]:

$$\nabla E(\mathbf{m}) = \sum_{i=1}^{N_s} \mathrm{Re}\left\{ \mathbf{U}_i^{\mathrm{T}} \frac{\partial \mathbf{S}^{\mathrm{T}}}{\partial \mathbf{m}} \mathbf{S}^{-1} \mathbf{r}_i^* \right\}, \tag{2.5}$$

where $\mathbf{U}_i$ is the forward-propagated wavefield from the i^{th} shot, $\mathbf{S}$ is wavefield modeling operator, $\mathbf{r}_i$ is the adjoint source with expression

$$r_{ij} = u_{ij} - d_{ij}. \tag{2.6}$$

We use a limited-memory variant of the quasi-Newton BFGS method known as the L-BFGS algorithm [1] to approximate the inverse of Hessian matrix $\mathbf{H}_n$ and line-search method to compute the model update step α_n:

$$\mathbf{m}_{n+1} = \mathbf{m}_n - \alpha_n \mathbf{H}_n^{-1} \nabla E(\mathbf{m}). \tag{2.7}$$

2.2 Amplitude-semblance objective function for the hybrid-domain FWI

To avoid source wavelet estimation during FWI, we define an amplitude-semblance function for the i^{th} common-shot gather data as

$$\varphi_i = \frac{\sum_j^{N_r} |u_{ij}| \cdot |d_{ij}|}{\|\mathbf{u}_i\| \|\mathbf{d}_i\|}, \tag{2.8}$$

where $|u_{ij}|$ and $|d_{ij}|$ are the amplitudes of synthetic and observed data as

$$|u_{ij}| = \sqrt{\left(\Re(u_{ij})\right)^2 + \left(\Im(u_{ij})\right)^2}, \tag{2.9}$$

and

$$|d_{ij}| = \sqrt{\left(\Re(d_{ij})\right)^2 + \left(\Im(d_{ij})\right)^2}. \tag{2.10}$$

$\|\mathbf{u}_i\| \|\mathbf{d}_i\|$ is a normalization factor defined as

$$\|\mathbf{u}_i\| \|\mathbf{d}_i\| = \sqrt{\sum_j^{N_r} |u_{ij}|^2} \sqrt{\sum_j^{N_r} |d_{ij}|^2}. \tag{2.11}$$

The amplitude semblance can be used to measure the similarity of synthetic and observed data. It reaches the maximum value of one when synthetic and observed data are identical, and is a value between zero and one if synthetic data deviate from observed data. Using the L_2 norm, we define our new amplitude-semblance objective function for the hybrid-domain FWI as

$$E_{AS}(\mathbf{m}) = \frac{1}{2} \sum_i^{N_s} (1 - \varphi_i)^2. \tag{2.12}$$

The new objective function in Eq. (2.12) is source independent. To demonstrate this feature, we rewrite Eq. (2.8) as

$$\varphi_i = \frac{\sum_j^{N_r} |g_{ij}^u||s_i^u| \cdot |g_{ij}^d||s_i^d|}{|s_i^u| \cdot \|\mathbf{g}_i^u\| \|\mathbf{g}_i^d\| \cdot |s_i^d|} = \frac{\sum_j^{N_r} |g_{ij}^u| \cdot |g_{ij}^d|}{\|\mathbf{g}_i^u\| \|\mathbf{g}_i^d\|}, \tag{2.13}$$

where $\|\mathbf{g}_i^u\| \|\mathbf{g}_i^d\|$ can be written as

$$\|\mathbf{g}_i^u\| \|\mathbf{g}_i^d\| = \sqrt{\sum_j^{N_r} |g_{ij}^u|^2} \sqrt{\sum_j^{N_r} |g_{ij}^d|^2}. \tag{2.14}$$

Eq. (2.13) indicates that the source effect, including the differences in amplitude and phase between synthetic and observed data, is removed from the objective function, and the objective function depends only on model parameters through Green's functions.

2.3 Gradient of the amplitude-semblance objective function

We obtain the gradient of the amplitude-semblance objective function with respect to the k^{th} model parameter m_k using

$$\frac{\partial E_{AS}(\mathbf{m})}{\partial m_k} = \sum_i^{N_s} (1-\varphi_i) \frac{\partial (1-\varphi_i)}{\partial m_k}, \tag{2.15}$$

where

$$\frac{\partial (1-\varphi_i)}{\partial m_k} = -\frac{\partial \frac{\sum_j^{N_r} |u_{ij}| \cdot |d_{ij}|}{\|\mathbf{u}_i\| \|\mathbf{d}_i\|}}{\partial m_k}. \tag{2.16}$$

Eq. (2.16) can be further expanded to

$$\frac{\partial (1-\varphi_i)}{\partial m_k} = -\left[\sum_j^{N_r} |d_{ij}| \|\mathbf{u}_i\|^2 \frac{\partial |u_{ij}|}{\partial m_k} - \sum_j^{N_r} \left(\sum_j^{N_r} |u_{ij}| \cdot |d_{ij}| \right) \cdot |u_{ij}| \frac{\partial |u_{ij}|}{\partial m_k} \right] \cdot \frac{1}{\|\mathbf{u}_i\|^3 \|\mathbf{d}_i\|}, \tag{2.17}$$

where the partial derivative of the amplitude spectrum is given by [5]

$$\frac{\partial |u_{ij}|}{\partial m_k} = |u_{ij}| \Re \left(\frac{1}{u_{ij}} \cdot \frac{\partial u_{ij}}{\partial m_k} \right). \tag{2.18}$$

Substituting Eq. (2.17) and (2.18) into Eq. (2.15) yields

$$\frac{\partial E_{AS}(\mathbf{m})}{\partial m_k} = \sum_i^{N_s} \sum_j^{N_r} \Re \left\{ (1-\varphi_i) \left[|u_{ij}||d_{ij}| \|\mathbf{u}_i\|^2 - \left(\sum_j^{N_r} |u_{ij}| \cdot |d_{ij}| \right) \cdot |u_{ij}|^2 \right] \times \frac{1}{u_{ij} \|\mathbf{u}_i\|^3 \|\mathbf{d}_i\|} \frac{\partial u_{ij}}{\partial m_k} \right\}. \tag{2.19}$$

We compute the gradient of the misfit function in Eq. (2.19) using the adjoint-state technique given by

$$\nabla E_{AS}(\mathbf{m}) = \sum_{i=1}^{N_s} \Re\left\{ \mathbf{U}_i^{\mathrm{T}} \frac{\partial \mathbf{S}^{\mathrm{T}}}{\partial \mathbf{m}} \mathbf{S}^{-1} \mathbf{r}_i \right\}, \tag{2.20}$$

where $\mathbf{r}_i$ is the adjoint source with expression

$$r_{ij} = (1-\varphi_i) \left[|u_{ij}||d_{ij}| \|\mathbf{u}_i\|^2 - \left(\sum_j^{N_r} |u_{ij}| \cdot |d_{ij}| \right) \cdot |u_{ij}|^2 \right] \frac{1}{u_{ij} \|\mathbf{u}_i\|^3 \|\mathbf{d}_i\|}. \tag{2.21}$$

2.4 Characteristics of the amplitude-semblance objective function

We use numerical modeling to study the characteristics of our amplitude-semblance objective function, and verify two fundamental characteristics. The first characteristic is whether the amplitude-semblance objective function is source independent, that is, if the source wavelet is incorrect, whether the amplitude-semblance objective function can reach the global minimum where the model is accurate. The other characteristic is whether the nonlinearity of the new inverse problem increases, that is, to obtain a stable inversion result, whether our amplitude-semblance FWI requires a more accurate initial model than the conventional waveform-residual-based FWI.

We use a model as shown in Fig. 1 consisting of a homogeneous background model with a velocity value of 2 km/s and a circular inclusion with a velocity value of 3 km/s to study the characteristics of our amplitude-semblance objective function. In the following numerical modeling, a point source is located at the center of the top surface of the model, and receivers are placed at the bottom side of the model. We generate transmission seismic data for the source with a Ricker time function. The center frequency of the Ricker wavelet is 10 Hz, a time delay is 0.1 s, and the amplitude is 1.0. We use these seismic data as data d in Eq. (2.8) for computing the amplitude semblance objective function in Eq. (2.12). We compute synthetic data u in Eq. (2.8) for different FWI initial velocity models in which the velocity perturbations in the circular inclusion are $\pm 20\%$ of its true velocity value, that is, the velocity values of the circular inclusion vary from 2.4 km/s to 3.6 km/s.

In the first numerical test, we study the characteristic of the our amplitude-semblance objective function for an incorrect source wavelet used for ASFWI forward modeling. When generating synthetic data u, we use a source wavelet with a center frequency of 9 Hz, a time delay of 0.12 s and an amplitude of 0.9, which are different from those parameters of the source wavelet used for generating data d. Then we compute the values of the amplitude-semblance objective function using Eq. (2.12), and display the relationship between the amplitude-semblance objective function and the FWI initial velocity as the red curve in Fig. 2a. For comparison, we show the relationship between the conventional waveform-residual objective function in (2.3) and the FWI initial velocity as the blue curve in Fig. 2a. The global minimum of the conventional objective function

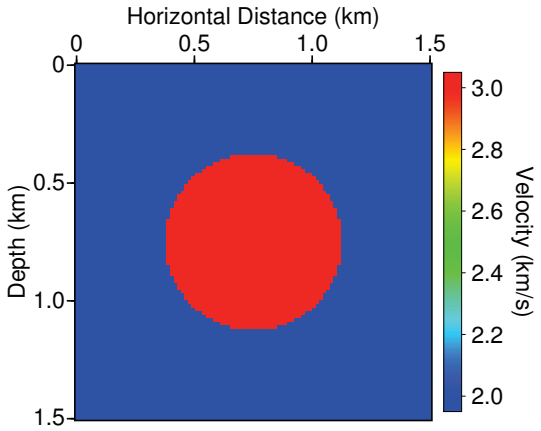

Figure 1: A model consists of a homogeneous background and a high-velocity circular inclusion at the center for studying the characteristics of the amplitude-semblance objective function.

vs the FWI initial velocity is at the velocity value of approximately 3.24 km/s, which is different from the true velocity value of 3.0 km/s. This is caused by the incorrect source wavelet used in the FWI forward modeling. This result means that the conventional FWI could converge to a wrong velocity model when using an incorrect source wavelet for the FWI forward problem. By contrast, our amplitude-semblance objective function behaves the quadric characteristic around the global minimum at the velocity value of 3.0 km/s, which is the same as the true velocity value. Therefore, our ASFWI could converge to a correct velocity model even using an incorrect source wavelet. In other words, our ASFWI is source-independent.

In the second numerical test, we study the characteristic of the our amplitude-semblance objective function with respect to the initial velocity when a correct source wavelet is used for ASFWI forward modeling. We compute data d and synthetic data u using the same source wavelet with a center frequency of 10 Hz, a time delay of 0.1 s, and an amplitude of 1.0. Then we compute the values of the amplitude-semblance objective function using Eq. (2.12), and display the relationship between the amplitude-semblance objective function and the FWI initial velocity as the red curve in Fig. 2b. For comparison, we show the relationship between the conventional waveform-residual objective function in (2.3) and the FWI initial velocity as the blue curve in Fig. 2b. For different FWI initial velocity models, the conventional and our amplitude-semblance objective functions behave almost the same quadric characteristic around their global minima at the velocity value of 3.0 km/s, which is the true velocity value of the circular inclusion. Therefore, when using the local-gradient-based inversion method, both the conventional FWI and our ASFWI could converge to the true velocity model. On the other hand, the regions of convergence and curvature around the global minima for these two objective functions are almost the same, which means the nonlinearity of the amplitude-semblance objective function does not increase compared to that of the conventional objective function. In other words, our amplitude-semblance FWI does not require a more accurate initial model compared

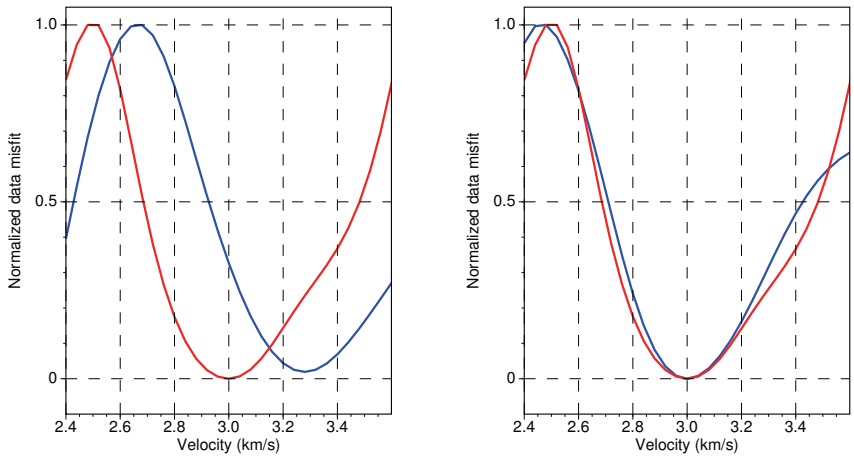

(a) Using an incorrect source wavelet (b) Using a correct source wavelet

Figure 2: Normalized data misfits vs the FWI initial velocity obtained with an incorrect source wavelet (a) and the correct source wavelet (b) for the conventional waveform-residual objective function (blue) and our new amplitude-semblance objective function (red).

to the conventional waveform-residual-based FWI, and the convergence rates for theses two methods are also almost the same when using the correct source wavelet.

3 Numerical examples

We use the Marmousi model to demonstrate the advantage of the source independent of our ASFWI method and compare the results with those obtained using the conventional FWI. Fig. 3 shows the Marmousi velocity model and the Gaussian-smoothed velocity model as the FWI initial model. The grid interval is 20 m in both the horizontal and vertical directions. We place 80 sources at the depth of 20 m with a source interval of 100 m. The receivers are located at the same depth with the sources and the receiver interval is 20 m. We generate data d using a Ricker source wavelet with a center frequency of 10 Hz, a time lag of 0.1 s and the maximum amplitude of 1.0.

We first conduct the conventional FWI and our ASFWI assuming the source wavelet is known, that is, using the same source wavelet for generating data d and for FWI/ASFWI forward modeling. In our hybrid time- and frequency-domain inversion, we use nine frequency components of data from 2 Hz to 20 Hz (2.0 Hz, 2.7 Hz, 3.6 Hz, 4.9 Hz, 6.6 Hz, 9.0 Hz, 12.1 Hz, 16.3 Hz and 20.0 Hz) with a frequency continuation strategy given by Sirgue and Pratt [16]. We perform inversion for 30 iterations for each frequency, and show the inversion results in Fig. 4. Both inversion results are almost the same. For quantitative comparison, we depict the vertical velocity profiles of the Marmousi model, the initial model, and the inverted models at horizontal locations of 3 km and 5 km in Fig. 5. Figs. 4 and 5 demonstrate that the inversion accuracy and resolution of the ASFWI

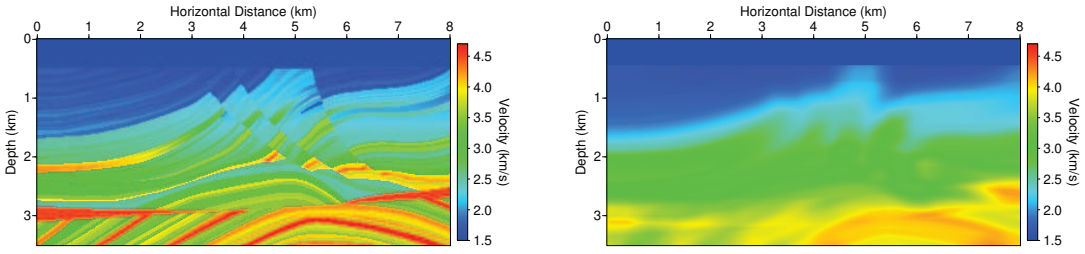

(a) Marmousi model

(b) Smoothed Marmousi model as FWI initial model

Figure 3: Marmousi velocity model (a) together with the initial model for FWI (b).

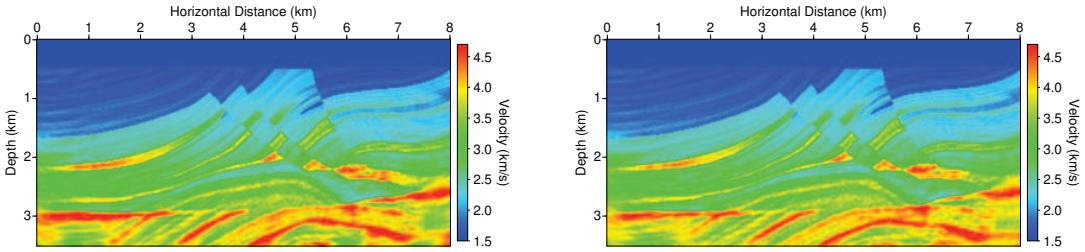

(a) FWI inverted model

(b) ASFWI inverted model

Figure 4: The inverted velocity models obtained using the conventional FWI (a) and our amplitude-semblance FWI (b) with the correct source wavelet. Both results are similar to each other.

result is comparable to those of the conventional FWI result when the source wavelet is known.

We then study the impact of inaccurate source wavelet on FWI and the capability of our source-independent ASFWI method to handle inaccurate source wavelets.

For the conventional FWI, we use a Ricker wavelet that is slightly different from the one used to generate data d. The source wavelet for FWI forward modeling to generate u has a center frequency of 9 Hz, a time lag of 0.11 s and an amplitude of 1.0.

For our source-independent ASFWI, we generate seismic data d using four different source wavelets as shown in Fig. 6. Each group of consecutive 20 sources uses one of these four source wavelets. As shown in Fig. 6, these four source wavelets are significantly different from one another, including the center frequency f_0, the time delay t_0 (or the source excitation time), the amplitude A, and the type of the source time function. In our ASFWI inversion, we use only one source wavelet in Fig. 6a for forward modeling.

The inversion result obtained using the conventional FWI and the inaccurate source wavelet as shown in Fig. 7a is much worse than that in Fig. 4a. Fig. 7a demonstrates that the source wavelet used in the conventional FWI plays a crucial role in inversion results. By contrast, our ASFWI result shown in Fig. 7b is almost the same as that in Fig. 4b. This inversion result manifests the source-independence characteristic of our ASFWI method.

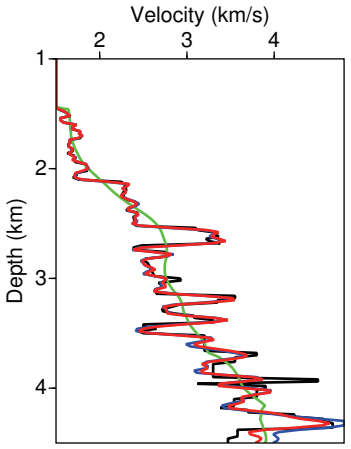

(a) Vertical velocity profiles at $x=3$ km

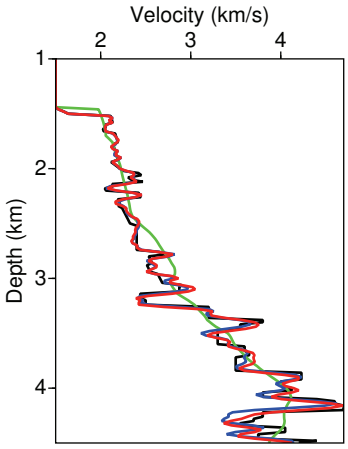

(b) Vertical velocity profiles at $x=5$ km

Figure 5: Comparison of vertical velocity profiles at the horizontal locations of (a) 3 km and (b) 5 km among: the true velocity model (black), the initial velocity model (green), the conventional FWI result (blue), and the ASFWI result (red) for the inversion results in Fig. 4. Both the blue and red curves behave mostly similar to each other.

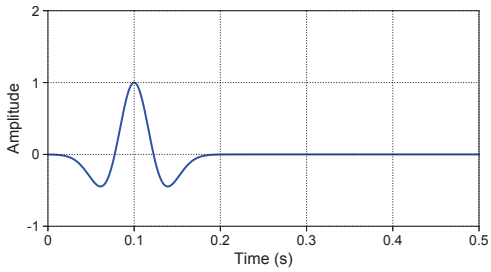

(a) Ricker wavelet: $f_0=10$ Hz, $t_0=0.1$ s and $A=1.0$

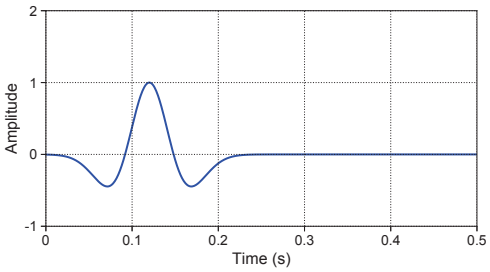

(b) Ricker wavelet: $f_0=8$ Hz, $t_0=0.12$ s and $A=1.0$

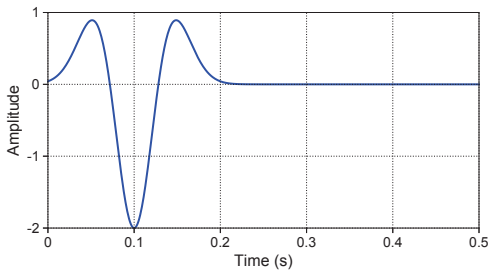

(c) Ricker wavelet: $f_0=10$ Hz, $t_0=0.1$ s and $A=-2.0$

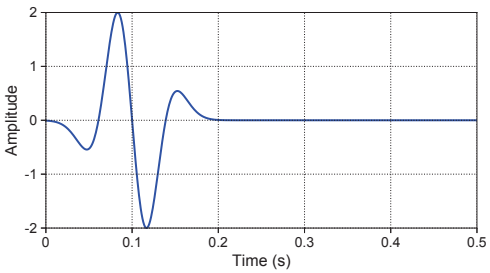

(d) Derivative of Ricker: $f_0=10$ Hz, $t_0=0.1$ s and $A=2.0$

Figure 6: (a) Ricker wavelet with a center frequency of 10 Hz, a time delay of 0.1 s, and an amplitude of 1.0; (b) Ricker wavelet with a center frequency of 8 Hz, a time delay of 0.12 s, and an amplitude of 1.0; (c) Ricker wavelet with a center frequency of 10 Hz, a time delay of 0.1 s, and an amplitude of -2.0; and (d) Time derivative of a Ricker wavelet with a center frequency of 10 Hz, a time delay of 0.1 s, and an amplitude of 2.0.

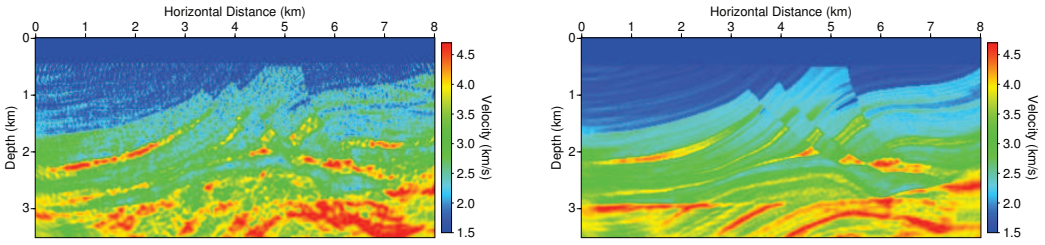

(a) FWI inverted model (b) ASFWI inverted model

Figure 7: (a) The conventional FWI obtained using small source-wavelet deviations results in a noisy, inaccurate inversion result. (b) Our amplitude-semblance FWI inversion for data with various source wavelets produces an accurate velocity model with greatly reduced inversion artifacts.

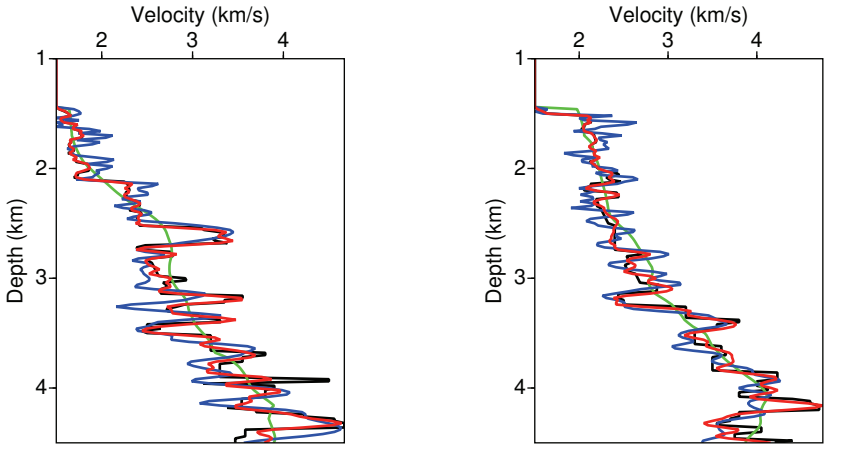

(a) Vertical velocity profiles at 3 km (b) Vertical velocity profiles at 5 km

Figure 8: Comparison of vertical velocity profiles at the horizontal locations of (a) 3 km and (b) 5 km among: the true velocity model (black), the initial velocity model (green), the conventional FWI result (blue), and the ASFWI result (red) for the inversion results in Fig. 7.

To quantitatively compare the inversion results in Fig. 7, we plot vertical velocity profiles at the horizontal positions of 3 km and 5 km in Fig. 8. Our ASFWI profiles in red are much closer to the true one in black than the conventional FWI profiles in blue.

4 Conclusions

We have developed a novel source-independent full-waveform inversion method using the amplitude-semblance objective function and a hybrid time- and frequency-domain inversion framework. The method can be used for both acoustic- and elastic-waveform inversion. Unlike conventional source-independent full-waveform inversion methods, the source-wavelet effect in our new method is alleviated without the need of reference traces. We have derived the formulation for computing the gradients of the amplitude-

semblance objective function with respect to model parameters in the hybrid time- and frequency-domain inversion framework. We have verified the source-independent characteristic of our new method using a model with a circular inclusion and the Marmousi model. The results show that, even without using an accurate source wavelet, our new full-waveform inversion produces accurate inversion results resembling to those obtained using a known source wavelet. Our new method provides a powerful tool for field data applications of full-waveform inversion without the need of source-wavelet estimation.

Acknowledgments

This work was supported by the U.S. Department of Energy (DOE) through the Los Alamos National Laboratory (LANL), which is operated by Triad National Security, LLC, for the National Nuclear Security Administration (NNSA) of U.S. DOE under Contract No. 89233218CNA000001. This research used resources provided by the LANL Institutional Computing Program, which is supported by the U.S. DOE NNSA under Contract No. 89233218CNA000001.

References

[1] R. Byrd, P. Lu, J. Nocedal, and C. Zhu. A limited memory algorithm for bound constrained optimization. *SIAM Journal on Scientific Computing*, 16(5):1190–1208, 1995.

[2] Y. Choi and T. Alkhalifah. Source-independent time-domain waveform inversion using convolved wavefields: Application to the encoded multisource waveform inversion. *Geophysics*, 76(5):R125–R134, 2011.

[3] Y. Choi, T. Alkhalifah, and B. DeVault. Application of the unwrapped phase inversion to land data without source estimation. *SEG Technical Program Expanded Abstracts 2015*, pages 1225–1229, 2015.

[4] Y. Choi and D.-J. Min. Source-independent elastic waveform inversion using a logarithmic wavefield. *Journal of Applied Geophysics*, 76:13 – 22, 2012.

[5] Y. Choi, C. Shin, D.-J. Min, and T. Ha. Efficient calculation of the steepest descent direction for source-independent seismic waveform inversion: An amplitude approach. *Journal of Computational Physics*, 208(2):455 – 468, 2005.

[6] R. Kamei, R. G. Pratt, and T. Tsuji. On acoustic waveform tomography of wide-angle OBS datastrategies for pre-conditioning and inversion. *Geophysical Journal International*, 194(2):1250–1280, 2013.

[7] R. Kamei, R. G. Pratt, and T. Tsuji. Misfit functionals in LaplaceFourier domain waveform inversion, with application to wideangle ocean bottom seismograph data. *Geophysical Prospecting*, 62(5):1054–1074, 2014.

[8] K. H. Lee and H. J. Kim. Sourceindependent fullwaveform inversion of seismic data. *Geophysics*, 68(6):2010–2015, 2003.

[9] K. T. Nihei and X. Li. Frequency response modelling of seismic waves using finite difference time domain with phase sensitive detection (td-psd). *Geophysical Journal International*, 169(3):1069–1078, 2007.

[10] S. Operto, J. Virieux, P. Amestoy, J.-Y. L'Excellent, L. Giraud, and H. B. H. Ali. 3d finite-difference frequency-domain modeling of visco-acoustic wave propagation using a massively parallel direct solver: A feasibility study. *Geophysics*, 72(5):SM195–SM211, 2007.
[11] R. G. Pratt. Seismic waveform inversion in the frequency domain, Part 1: Theory and verification in a physical scale model. *Geophysics*, 64(3):888–901, 1999.
[12] R. G. Pratt, C. Shin, and G. J. Hick. GaussNewton and full Newton methods in frequencyspace seismic waveform inversion. *Geophysical Journal International*, 133(2):341–362, 1998.
[13] C. Ravaut, S. Operto, L. Improta, J. Virieux, A. Herrero, and P. Dell'Aversana. Multiscale imaging of complex structures from multifold wideaperture seismic data by frequencydomain fullwaveform tomography: application to a thrust belt. *Geophysical Journal International*, 159(3):1032–1056, 2004.
[14] C. Shin, W. Ha, and Y. Kim. Subsurface model estimation using laplace-domain inversion methods. *The Leading Edge*, 32(9):1094–1099, 2013.
[15] L. Sirgue, J. T. Etgen, and U. Albertin. 3D frequency domain waveform inversion using time domain finite difference methods. In *Extended Abstracts of the 70th EAGE Conference and Exhibition*, 2008.
[16] L. Sirgue and R. G. Pratt. Efficient waveform inversion and imaging: A strategy for selecting temporal frequencies. *Geophysics*, 69(1):231–248, 2004.
[17] D. Sun, K. Jiao, X. Cheng, and D. Vigh. Compensating for source and receiver ghost effects in full waveform inversion and reverse time migration for marine streamer data. *Geophysical Journal International*, 201(3):1507–1521, 2015.
[18] W. W. Symes. Reverse time migration with optimal checkpointing. *Geophysics*, 72(5):SM213–SM221, 2007.
[19] S. Tan and L. Huang. An efficient finite-difference method with high-order accuracy in both time and space domains for modelling scalar-wave propagation. *Geophysical Journal International*, 197(2):1250–1267, 2014.
[20] S. Tan and L. Huang. Reducing the computer memory requirement for 3d reverse-time migration with a boundary-wavefield extrapolation method. *Geophysics*, 79(5):S185–S194, 2014.
[21] S. Tan and L. Huang. A staggered-grid finite-difference scheme optimized in the timespace domain for modeling scalar-wave propagation in geophysical problems. *Journal of Computational Physics*, 276:613 – 634, 2014.
[22] A. Tarantola. Inversion of seismic reflection data in the acoustic approximation. *Geophysics*, 49(8):1259–1266, 1984.
[23] J. Virieux and S. Operto. An overview of full-waveform inversion in exploration geophysics. *Geophysics*, 74(6):WCC1–WCC26, 2009.
[24] Z. Wu and T. Alkhalifah. Efficient scattering-angle enrichment for a nonlinear inversion of the background and perturbations components of a velocity model. *Geophysical Journal International*, 210(3):1981–1992, 2017.
[25] K. Xu, S. A. Greenhalgh, and M. Wang. Comparison of source-independent methods of elastic waveform inversion. *Geophysics*, 71(6):R91–R100, 2006.
[26] Q. Zhang, H. Zhou, Q. Li, H. Chen, and J. Wang. Robust source-independent elastic fullwaveform inversion in the time domain. *Geophysics*, 81(2):R29–R44, 2016.
[27] B. Zhou and S. A. Greenhalgh. Crosshole seismic inversion with normalized fullwaveform amplitude data. *Geophysics*, 68(4):1320–1330, 2003.
[28] C. Zhou, G. T. Schuster, S. Hassanzadeh, and J. M. Harris. Elastic wave equation traveltime and waveform inversion of crosswell data. *Geophysics*, 62(3):853–868, 1997.